Mechanics of Advanced Composite Structures

Journal homepage: https://macs.semnan.ac.ir/

Semnan University

ISSN: 2423-7043

Research Article

Nonlinear Free Vibration of Fluid-Filled Hyperelastic Cylindrical Shells Using Novozhilov Theory and Multiple Scales Method

Saboor Savafi, Korosh Khorshidi*

Department of Mechanical Engineering, Faculty of Engineering, Arak University, Arak, 38156-88349, Iran

ARTICLE INFO

Article history:

Received:
Revised:
Accepted:

Keywords:

Fluid-structure interaction;
Novozhilov theory;
Multiple-scale method;
Hardening and softening behavior.

ABSTRACT

This study investigates the nonlinear free vibration of thin, fluid-filled cylindrical shells made of hyperelastic material. Utilizing the Mooney-Rivlin constitutive model, the equations of motion are derived via Lagrange's equation, accounting for potential, kinetic, and damping energy. To ensure a higher level of accuracy and precision in capturing the shell's kinematics, the analysis employs Novozhilov's nonlinear shell theory, which incorporates higher-order geometric terms often neglected in standard analytical approaches. This theoretical framework constitutes the core novelty of the present work, enabling a more rigorous investigation compared to existing studies that rely on simplified shell theories. The multiple-scale method is employed to obtain an analytical solution based on this refined model. Key findings include: (1) the fundamental vibration mode is identified as (1,4), corresponding to one longitudinal half-wave and four circumferential waves; (2) the presence of fluid markedly reduces the natural frequency due to added mass effects; (3) the system generally exhibits hardening behavior, which intensifies with increased fluid content and higher circumferential wave numbers; however, a transition to softening behavior occurs when the shell length is four times the radius (β=0.25); and (4) a weakly hardening response is observed when shell length equals its radius (β=1). Results are validated against finite element simulations in ANSYS and compared with existing literature, offering valuable insights for the design and vibration control of soft fluid-structure systems in applications such as soft robotics and biomedical implants.

1. Introduction

Materials that exhibit large, recoverable deformations under small forces are classified as viscoelastic, Green elastic, or hyperelastic [1]. Their stress-strain relationship is far more complex than that of conventional elastic materials, requiring non-linear models for accurate description, as Hooke's law is insufficient [2]. Several prominent models have been developed to characterize this behavior, including the Mooney-Rivlin (1940), Neo-Hookean (1948), and Yeoh (1993) models. These frameworks describe material properties using the invariants of the left Cauchy-Green tensor and have been applied in various fields; for instance, non-linear constitutive models are used to analyze the mechanical behavior of human

* **Corresponding author.**
E-mail address: *k-khorshidi@araku.ac.ir*

Cite this article as:

Savvafi, S. and Khorshidi, K., 2027. Nonlinear Free Vibration of Fluid-Filled Hyperelastic Cylindrical Shells Using Novozhilov Theory and Multiple Scales Method. *Mechanics of Advanced Composite Structures*, 14(1), pp. xxx-xxx.
https://doi.org/10.22075/MACS.2025.39313.2050

arteries [3]. The Mooney-Rivlin model is particularly renowned for its simplicity and effectiveness in modeling a wide range of hyperelastic materials undergoing deformations of up to 200% [4].

The application of hyperelastic materials has expanded significantly in recent years, especially in biomechanics and soft robotics [5]. This broad utility necessitates a deep understanding of their mechanical phenomena, leading to a substantial increase in research. Consequently, numerous studies now investigate specific behaviors, such as vibration in hyperelastic structures like beams, plates, and shells [4].

Research on hyperelastic beams and plates includes studies on their nonlinear dynamics. Khaniki et al. [6] modeled hyperelastic beams using various energy density models to analyze vibration and the impact of parameters like axial velocity. Chen et al.[7] developed a neo-Hookean beam model, studying nonlinear free vibrations that exhibit chaotic and quasi-periodic responses. Breslavsky et al.[8] analyzed plates using Neo-Hookean, Mooney-Rivlin, and Ogden models, validating findings with finite element software. Khaniki et al. [9] examined plate dynamics and mass sensitivity with Mooney-Rivlin and von-Kármán models, corroborating results experimentally and theoretically. This focus on complex behavior extends to advanced composites, such as in the vibration analysis of functionally graded carbon nanotube-reinforced shells with piezoelectric layers in thermal environments [10], underscoring the relevance of multi-physics coupling.

The study of vibrations in cylindrical structures reveals that a significant portion of research focuses on large-amplitude vibrations in shells, which inherently requires nonlinear analysis. Investigators have employed a range of theories for this purpose, including the nonlinear theories of Donnell, Sanders-Koiter, Flügge-Lur'e-Byrne, and Novozhilov, as well as higher-order shear deformation theory [11]. The governing equations are typically derived using either Hamilton's principle or the more flexible Lagrange equation. Beyond the core theory, research often explores critical factors like geometric imperfections, internal fluid presence, and thermal effects on the system's behavior.

Notable contributions in this field include the work of Amabili [12], who compared four nonlinear shell theories to analyze the dynamics of perfect and imperfect circular cylindrical shells under harmonic excitation, considering influences such as axial load and fluid interaction. In another study, Amabili [13] examined geometrically nonlinear forced vibrations in laminated shells, identifying complex dynamic responses including internal resonances and quasi-periodic vibrations. A broader review by Alijani and Amabili [14] encompassed nonlinear vibrations of shells made from various advanced materials, including hyperelastic composites, while addressing multiphysics couplings like fluid-structure interaction and thermal loads. Further research by Mohammadi et al. [15] investigated the nonlinear vibrations of axially moving cylindrical shells, and Zippo et al. [16] studied the temperature-sensitive nonlinear dynamics of a polymeric cylindrical shell under harmonic excitation, demonstrating that temperature significantly alters its instability regions.

The analysis then shifts specifically to the vibration of hyperelastic cylindrical shells, a problem that is fundamentally nonlinear in nature due to the constitutive behavior of the material. Studies in this domain primarily investigate phenomena such as the hardening and softening responses in free vibration, the occurrence of internal resonance, and forced vibration dynamics. A foundational reference in this area is Amabili's work [17], which analyzes vibrations in multi-layer hyperelastic shells using computational methods implemented in AUTO 97 software [18]. For analytical treatment, perturbation methods—including techniques such as direct expansion, averaging, Lindstedt-Poincaré, and the method of multiple time scales—are widely employed. Among these, the multiple time scales method [19, 20] is particularly valued for its broad applicability and its ability to decouple the governing nonlinear equations. The utility of the multiple time scales method is well demonstrated in its application to problems exhibiting strong geometric nonlinearity, such as in deriving exact solutions for the nonlinear free transverse vibration of beams [21]. Its robustness has established it as a standard technique for solving nonlinear vibration equations and for investigating internal resonance phenomena. Specific research on hyperelastic cylindrical shells includes work by Arani et al. [22], who analyzed nonlinear vibrations under radial harmonic excitation using a Mooney-Rivlin model within Donnell's theory, validating their results with finite element analysis. A subsequent study by the same authors [23] examined the influence of initial geometric imperfections, finding they elevate the natural frequency and induce combined softening and hardening peaks in the amplitude response. Further, Saeidiha et al. [24] investigated primary resonance in thin-walled shells, analyzing how excitation amplitude and geometric ratios affect the frequency-amplitude relationship. Continuing this line of inquiry, further research delves deeper into complex nonlinear dynamics. Zhao et al. [25] confirmed a

2:1 internal resonance in thin-walled Mooney-Rivlin shells, demonstrating that the resonance range widens with excitation amplitude and noting the occurrence of double-jumping phenomena. Zhang et al.[26] focused on the vibration modes of rubber cylindrical shells, highlighting a significant sensitivity to the thickness-radius ratio and comparing coupled versus uncoupled modal responses. Expanding on the role of imperfections, Zhang et al. [27] analyzed how initial geometric defects influence resonant peaks and mode synchronization under harmonic excitation, ultimately leading to chaotic vibrations. Finally, extending the analysis to multiphysics interactions, Xu et al. [28] investigated internal resonance in shells subjected to time-varying temperature fields. Their work, which employed harmonic balance and arc-length continuation methods, revealed that both structural and thermal parameters critically affect the resonance range and stability, particularly for a 3:1 internal resonance.

While recent work has examined the nonlinear vibrations of fluid-filled hyperelastic shells using Donnell-type theories and harmonic balance methods [29], the present study distinguishes itself by employing the more geometrically rigorous Novozhilov theory. Combined with the method of multiple scales, this approach aims to derive closed-form analytical expressions for the nonlinear frequency-amplitude relationship, with a specific focus on free vibration and the fundamental transitions between hardening and softening behavior induced by the presence of a contained fluid.

This investigation is situated within a broader research context on the dynamics of advanced shell structures. Significant studies have analyzed the free vibration of adhesively bonded joints in laminated conical and cylindrical shells, detailing the influence of adhesive properties and geometric parameters [30-32]. Research has also expanded to multi-physics couplings, exploring the effects of electro-magnetic potentials on rotating functionally graded shells [33] and size-dependent vibrations in fiber-metal laminates at micro and nano scales [34]. Collectively, these works highlight a strong focus on the dynamics of complex, layered shell systems. However, they predominantly address linear or geometrically nonlinear vibrations of traditional elastic or composite materials. A distinct gap remains in the analytical investigation of shells exhibiting both the constitutive nonlinearity of hyperelastic materials and the coupled dynamic effect of a stationary internal fluid, which the present work seeks to address.

Finally, to address the objective of investigating fluid interaction within a hyperelastic cylinder, a review of relevant literature was essential. This review first considered foundational studies on the vibrations of fluid-filled cylindrical shells in general. Pioneering work in fluid-structure interaction for cylindrical systems is attributed to Païdoussis [35]. A comprehensive review by Amabili and Païdoussis [36] further details the geometrically nonlinear vibrations of circular shells and panels, analyzing the distinct effects of contained and flowing fluids on free and forced vibrations, stability, and dynamic response. This established body of work provides the essential context for the present study's focus on the unique coupled dynamics of a stationary fluid within a hyperelastic shell.

The fluid-structure interaction for cylindrical systems can be analyzed under diverse conditions, depending on whether the fluid is internal or external and whether it is stationary or flowing [11]. Within the specific context of hyperelastic cylinders, several key investigations inform the present study. Breslavsky et al. examined the static and dynamic responses of hyperelastic shells under pressure, noting significant material-dependent behavior at moderate strains and complex nonlinear dynamics in resonant regimes. Further, Zhang et al. [37] analyzed the resonant responses of graphene oxide-reinforced hyperelastic shells containing flowing fluid under harmonic excitation, detailing how reinforcement parameters and fluid velocity influence natural frequencies and can induce chaotic vibrations. These studies establish a precedent for analyzing coupled fluid-hyperelastic systems but primarily address flowing fluid or specific composite reinforcements. The present work thus focuses on the distinct scenario of a stationary fluid interacting with a homogeneous hyperelastic shell to isolate and characterize its fundamental nonlinear dynamic effects.

This research analyzes the nonlinear free vibration characteristics of thin-walled cylindrical shells composed of hyperelastic material and containing a stationary fluid. The Mooney-Rivlin constitutive model is applied, and the governing equations are formulated using Lagrange's equation, incorporating potential, kinetic, and damping energy components. A central contribution of this work is the adoption of Novozhilov's nonlinear shell theory to describe the kinematics. This theory provides enhanced geometric accuracy by retaining higher-order terms often omitted in more common analytical models, thereby forming a novel and more rigorous theoretical foundation for the problem. The analytical solution is derived via the multiple-scale method applied to this refined formulation. The principal findings of the study

are: (1) the fundamental vibration mode is characterized as (1,4), involving one longitudinal half-wave and four circumferential waves; (2) the contained fluid significantly lowers the natural frequency as a result of added mass; (3) the system predominantly displays hardening nonlinearity, which strengthens with greater fluid fill levels and higher circumferential wave numbers, though a distinct transition to softening behavior is identified when the shell length is four times the radius (β=0.25); and (4) a weakly hardening response is observed when the shell length equals its radius (β=1). Validation through finite element analysis in ANSYS and comparison with prior literature confirms the model's accuracy. These results provide critical insights for the design and dynamic management of soft fluid-structure systems, with direct relevance to fields such as soft robotics and biomedical engineering.

2. Mathematical model and description of motion:

2.1. Structural relations:

Figure 1 illustrates a thin-walled cylindrical shell composed of incompressible hyperelastic material containing static fluid. To simplify the analysis of cylindrical structures, a cylindrical coordinate system is employed, where x, θ, and z represent the axial, circumferential, and radial (normal) coordinates, respectively. As shown in Figure 1, the shell's mean radius, thickness, and length are denoted by R, h, and L, respectively. The coordinates (u, v, w) signify the displacements of a point on the shell's middle surface in the axial, circumferential, and radial directions. Meanwhile, (u_1, u_2, u_3) represent the displacements of any arbitrary point within the shell wall.

According to the Kirchhoff-Love assumption, the displacement at any arbitrary point on the shell can be described based on the displacement of a point on the middle surface, as expressed in Eqs. (1) [38].

$$u_1 = u - z\frac{\partial w}{\partial x}, \tag{1a}$$

$$u_2 = v - \frac{z}{R}\frac{\partial w}{\partial \theta}, \tag{1b}$$

$$u_3 = w. \tag{1c}$$

Based on Novozhilov's general nonlinear theory for thin shells, the strain components at an arbitrary distance z from the mid-surface are expressed as the sum of the mid-surface strains and bending contributions associated with changes in curvature [39]:

$$\varepsilon_{xx} = \varepsilon_{x,0} + zk_x$$

$$\varepsilon_{\theta\theta} = \varepsilon_{\theta,0} + zk_\theta$$

$$\varepsilon_{x\theta} = \varepsilon_{x\theta,0} + zk_{x\theta}$$

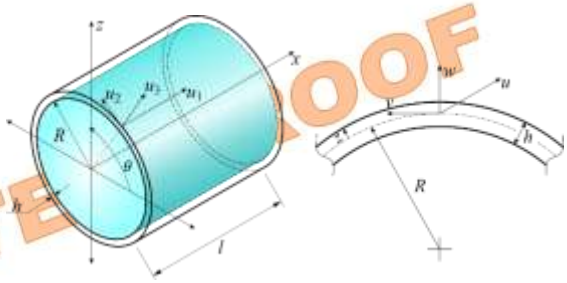

Fig. 1. Cylindrical Coordinates for a Thin-Walled Cylindrical Shell Containing Static Fluid

For thin, geometrically perfect cylindrical shells, these relations can be explicitly written in terms of the mid-surface displacement components as follows [39]:

$$\varepsilon_{xx} = \frac{\partial u}{\partial x} + \frac{1}{2}\left[\left(\frac{\partial u}{\partial x}\right)^2 + \left(\frac{\partial v}{\partial x}\right)^2 + \left(\frac{\partial w}{\partial x}\right)^2\right] - z\frac{\partial^2 w}{\partial x^2}, \tag{2a}$$

$$\varepsilon_{\theta\theta} = \frac{\partial v}{R\partial\theta} + \frac{w}{R} + \frac{1}{2R^2}\left[\left(\frac{\partial u}{\partial\theta}\right)^2 + \left(\frac{\partial v}{\partial\theta} + w\right)^2 + \left(\frac{\partial w}{\partial\theta} - v\right)^2\right] + z\left(\frac{\partial u}{R\partial x} - \frac{\partial^2 w}{R^2\partial\theta^2} + \frac{\partial v}{R^2\partial\theta}\right), \tag{2b}$$

$$\gamma_{x\theta} = \frac{\partial v}{\partial x} + \frac{\partial u}{R\partial\theta} + \frac{1}{R}\left[\frac{\partial u}{\partial x}\frac{\partial u}{\partial\theta} + \frac{\partial v}{\partial x}\left(\frac{\partial v}{\partial\theta} + w\right) + \frac{\partial w}{\partial x}\left(\frac{\partial w}{\partial\theta} - v\right)\right] + z\left[-2\frac{\partial^2 w}{R\partial x\partial\theta} - \frac{\partial u}{R^2\partial\theta} + \frac{\partial v}{R\partial x}\right]. \tag{2c}$$

These expressions represent the nonlinear strain–displacement relations derived from Novozhilov's theory, incorporating both membrane and bending effects in thin cylindrical shells.

2.2. Hyperelastic constitutive relations

The constitutive behavior of the incompressible hyperelastic material is described by the Mooney-Rivlin model. Its strain energy density function W is defined as a function of the first and second invariants (I_1, I_2)

of the left Cauchy-Green deformation tensor, as specified in Eq. (3) [40]:

$$W = C_{10}(I_1 - 3) + C_{01}(I_2 - 3) + \frac{1}{D}(J-1)^2 \quad (3)$$

The parameters C_{10} and C_{01} are material constants obtained experimentally. The terms I_1 and I_2 represent the first and second invariants of the left Cauchy-Green deformation tensor, $\boldsymbol{C}$. The coefficient D is a compressibility parameter, and J is the determinant of the deformation gradient, which defines the volume change.

The Green-Lagrange strain tensor ($\boldsymbol{E}$) for the cylinder is defined in Eq. (4a). The Cauchy-Green deformation tensor $\boldsymbol{C}$ is subsequently derived from the strain tensor $\boldsymbol{E}$ and the identity tensor $\boldsymbol{I}$, as shown in Eqs. (4b) and (4c) [22]:

$$\boldsymbol{E} = \frac{1}{2}\begin{bmatrix} 2\varepsilon_{xx} & \gamma_{x\theta} & 0 \\ \gamma_{x\theta} & 2\varepsilon_{\theta\theta} & 0 \\ 0 & 0 & 2\varepsilon_{zz} \end{bmatrix} \quad (4a)$$

$$\boldsymbol{C} = 2\boldsymbol{E} + \boldsymbol{I} \quad (4b)$$

$$\boldsymbol{C} = \begin{bmatrix} 2\varepsilon_{xx}+1 & 2\varepsilon_{x\theta} & 0 \\ 2\varepsilon_{x\theta} & 2\varepsilon_{\theta\theta}+1 & 0 \\ 0 & 0 & 2\varepsilon_{zz}+1 \end{bmatrix} \quad (4c)$$

$and\ \gamma_{x\theta} = 2\varepsilon_{x\theta}$

The first and second invariants of the Cauchy-Green deformation tensor are defined as:[41]:

$$I_1 = Tr(\boldsymbol{C}) = 2(\varepsilon_{xx} + \varepsilon_{\theta\theta} + \varepsilon_{zz}) + 3 \quad (5a)$$

$$\begin{aligned} I_2 = \frac{1}{2}(Tr(\boldsymbol{C})^2 - Tr(\boldsymbol{C}^2)) \\ = 4(\varepsilon_{xx} + \varepsilon_{\theta\theta} + \varepsilon_{zz} \\ + \varepsilon_{\theta\theta}\varepsilon_{xx} + \varepsilon_{\theta\theta}\varepsilon_{zz} + \varepsilon_{xx}\varepsilon_{zz}) \\ - 4\varepsilon_{x\theta}^2 + 3 \end{aligned} \quad (5b)$$

$$\begin{aligned} I_3 = J = det(\boldsymbol{C}) = (1 + 2\,\varepsilon_{zz})(1 + 2\varepsilon_{xx} \\ - 4\varepsilon_{x\theta}^2 + 2\varepsilon_{\theta\theta} + 4\varepsilon_{xx}\varepsilon_{\theta\theta}) \end{aligned} \quad (5c)$$

The incompressibility condition requires that $J = 1$. This constraint allows the normal strain ε_{zz} in the thickness direction to be expressed in terms of the in-plane strains ε_{xx}, $\varepsilon_{\theta\theta}$, and $\varepsilon_{x\theta}$.

$$\varepsilon_{zz} = \frac{-\varepsilon_{xx} + 2\varepsilon_{x\theta}^2 - \varepsilon_{\theta\theta} - 2\varepsilon_{xx}\varepsilon_{\theta\theta}}{1 + 2\varepsilon_{xx} - 4\varepsilon_{x\theta}^2 + 2\varepsilon_{\theta\theta} + 4\varepsilon_{xx}\varepsilon_{\theta\theta}} \quad (6)$$

The complexity of the integrals arising from the direct application of Eq. (6) necessitates an alternative approach. Consequently, Eq. (6) is replaced by its multivariate Taylor series expansion about the undeformed state (ε_{xx}, $\varepsilon_{\theta\theta}$, and $\varepsilon_{x\theta}$) up to the fourth order. This approximation is well-suited for modeling the moderate nonlinearities considered in this analysis [39]. Subsequently, this expansion is substituted, together with Eqs. (5a) and (5b), into the strain energy function defined in Eq. (3), resulting in the following expression:

$$\begin{aligned} W = C_{10}(&4\varepsilon_{xx}^2 - 8\varepsilon_{xx}^3 + 16\varepsilon_{xx}^4 + 16\varepsilon_{x\theta} \\ &+ 4\varepsilon_{x\theta}^2 - 16\varepsilon_{xx}\varepsilon_{x\theta}^2 \\ &+ 48\varepsilon_{xx}^2\varepsilon_{x\theta}^2 + 16\varepsilon_{x\theta}^4 \\ &+ 68\varepsilon_{xx}\varepsilon_{\theta\theta} - 8\varepsilon_{xx}^2\varepsilon_{\theta\theta} \\ &+ 16\varepsilon_{xx}^3\varepsilon_{\theta\theta} - 16\varepsilon_{x\theta}^2\varepsilon_{\theta\theta} \\ &+ 4\varepsilon_{\theta\theta}^2 - 8\varepsilon_{xx}\varepsilon_{\theta\theta}^2 \\ &+ 16\varepsilon_{xx}^2\varepsilon_{\theta\theta}^2 + 48\varepsilon_{x\theta}^2\varepsilon_{\theta\theta}^2 \\ &- 8\varepsilon_{\theta\theta}^3 + 16\varepsilon_{xx}\varepsilon_{\theta\theta}^3 + 16\varepsilon_{\theta\theta}^4) \\ &+ C_{01}(4\varepsilon_{xx}^2 - 8\varepsilon_{xx}^3 + 16\varepsilon_{xx}^4 \\ &+ 32\varepsilon_{xx}^5 + 32\varepsilon_{x\theta} + 32\varepsilon_{xx}\varepsilon_{x\theta} \\ &+ 4\varepsilon_{x\theta}^2 - 24\varepsilon_{xx}\varepsilon_{x\theta}^2 \\ &+ 64\varepsilon_{xx}^2\varepsilon_{x\theta}^2 + 96\varepsilon_{xx}^3\varepsilon_{x\theta}^2 \\ &+ 32\varepsilon_{x\theta}^4 + 32\varepsilon_{xx}\varepsilon_{x\theta}^4 \\ &+ 132\varepsilon_{xx}\varepsilon_{\theta\theta} + 128\varepsilon_{xx}^2\varepsilon_{\theta\theta} \\ &+ 64\varepsilon_{xx}^4\varepsilon_{\theta\theta} + 32\varepsilon_{x\theta}\varepsilon_{\theta\theta} \\ &- 24\varepsilon_{x\theta}^2\varepsilon_{\theta\theta} - 64\varepsilon_{xx}\varepsilon_{x\theta}^2\varepsilon_{\theta\theta} \\ &+ 96\varepsilon_{xx}^2\varepsilon_{x\theta}^2\varepsilon_{\theta\theta} + 32\varepsilon_{x\theta}^4\varepsilon_{\theta\theta} \\ &+ 4\varepsilon_{\theta\theta}^2 + 128\varepsilon_{xx}\varepsilon_{\theta\theta}^2 \\ &+ 64\varepsilon_{xx}^3\varepsilon_{\theta\theta}^2 + 64\varepsilon_{x\theta}^2\varepsilon_{\theta\theta}^2 \\ &+ 96\varepsilon_{xx}\varepsilon_{x\theta}^2\varepsilon_{\theta\theta}^2 - 8\varepsilon_{\theta\theta}^3 \\ &+ 64\varepsilon_{xx}^2\varepsilon_{\theta\theta}^3 + 96\varepsilon_{x\theta}^2\varepsilon_{\theta\theta}^3 \\ &+ 16\varepsilon_{\theta\theta}^4 + 64\varepsilon_{xx}\varepsilon_{\theta\theta}^4 \\ &+ 32\varepsilon_{\theta\theta}^5) \end{aligned} \quad (7)$$

While the strain energy expansion includes higher-order terms, the equations of motion are derived by retaining nonlinearities up to the third order (cubic) in the generalized coordinates. This is a standard and justified reduction for modeling moderate amplitude vibrations, as the dominant nonlinear phenomena are captured by cubic terms, ensuring analytical tractability while maintaining accuracy [42].

2.3. Developing the equations of motion:

The governing equations of motion are derived by applying Lagrange's equation, which for this system takes the following form [11]:

$$\frac{d}{dt}\left(\frac{\partial L}{\partial \dot{q}_i}\right) - \frac{\partial L}{\partial q_i} = \frac{\partial W_e}{\partial q_i} - \frac{\partial W_d}{\partial \dot{q}_i} \quad i = 1,2,\ldots \quad (8)$$

The Lagrangian L of the system is defined as $L = K - P$, where K and P represent the total kinetic and potential energy, respectively. In Eq. (8), W_e denotes the work done by external forces, and W_d is the dissipation function due to damping.

The kinetic energy for the thin circular cylindrical shell is expressed by Eq. (9) [11], derived under the standard shell theory assumptions of neglecting rotary inertia while retaining in-plane inertia. In this formulation, ρ signifies the density of the hyperelastic material, and the overdot notation indicates a derivative with respect to time.

$$K = \frac{1}{2}\rho R \int_0^l \int_0^{2\pi} \int_{-\frac{h}{2}}^{\frac{h}{2}} (\dot{u}_1^2 + \dot{u}_2^2 + \dot{u}_3^2) dz d\theta dx \quad (9)$$

The potential energy and the damping force are obtained from Eqs. (10) and (11), respectively. As this study focuses on free vibration, the external force is neglected ($W_e = 0$). The generalized coordinate vector q_i is defined as: $q_i = [u_{mn}, u_{m0}, v_{mn}, v_{m0}, w_{mn}, w_{m0}]^T$ [43]

$$P = \int_0^l \int_0^{2\pi} \int_{-\frac{h}{2}}^{\frac{h}{2}} WR \, dz d\theta dx \quad (10)$$

$$W_d = \frac{1}{2} c_d \int_0^{2\pi} \int_0^l (\dot{u}^2 + \dot{v}^2 + \dot{w}^2) R \, dx d\theta \quad (11)$$

Equation (11), commonly referred to as Rayleigh's dissipation function, models the system's energy dissipation mechanism. In this formulation, c_d denotes the viscous damping coefficient, which is treated as an intrinsic material property [24].

In practical engineering applications, the support conditions for cylindrical shells are frequently idealized as simply supported. Consequently, a wide range of thin-walled cylinder problems can be accurately modeled using simply supported boundary conditions[17], defined mathematically by Eqs. (12):[38]:

$$v = w = 0, \qquad \frac{\partial^2 v}{\partial x^2} = \frac{\partial^2 w}{\partial x^2} = 0, \qquad x = 0, l \quad (12)$$

The displacements u, v, and w represent the components of a point on the shell's mid-surface in the axial, circumferential, and radial directions, respectively. The vibration response of the shell is characterized by its mode shapes, which are defined by two parameters: the number of circumferential waves n, and the number of longitudinal half-waves m, as illustrated in Figure 2. These modes are broadly categorized as axisymmetric ($n = 0$) or asymmetric ($n > 0$), regardless of the value of m.

As the longitudinal half-wave number m must be a non-zero integer, the displacement field is approximated by a series expansion of trial functions, given in Eqs. (13)[25] :

$$u(x,\theta,t) = \sum_{m=1}^{M_1} \sum_{n=1}^{N_1} u_{mn}(t) \cos(n\theta) \cos(\lambda_m x) + \sum_{m=1}^{M_1} u_{m0} \cos(\lambda_m x) \quad (13a)$$

$$v(x,\theta,t) = \sum_{m=1}^{M_1} \sum_{n=1}^{N_1} v_{mn}(t) \sin(n\theta) \sin(\lambda_m x) + \sum_{m=1}^{M_1} v_{m0} \sin(\lambda_m x) \quad (13b)$$

$$w(x,\theta,t) = \sum_{m=1}^{M_1} \sum_{n=1}^{N_1} w_{mn}(t) \cos(n\theta) \sin(\lambda_m x) + \sum_{m=1}^{M_1} w_{m0} \sin(\lambda_m x) \quad (13c)$$

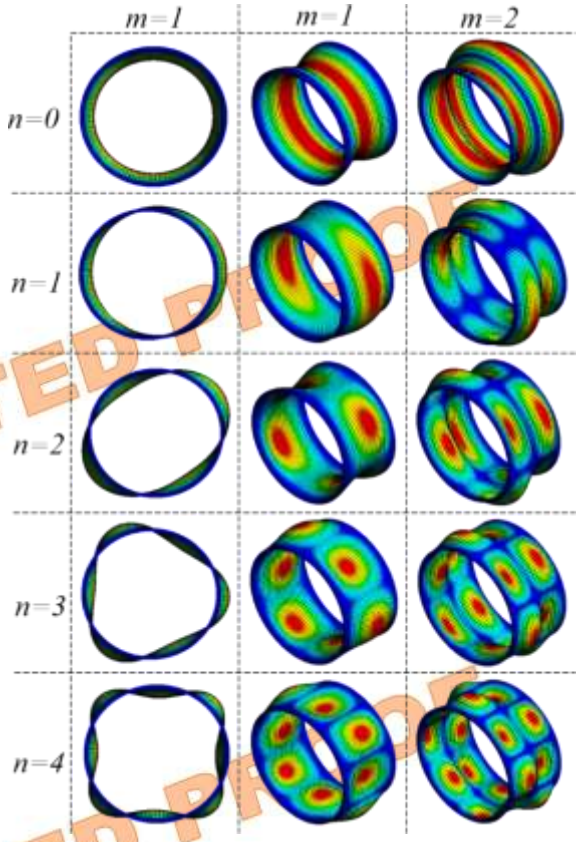

Fig. 2. The mode shapes in the cylindrical shell are defined based on the circumferential wave number (n) and the longitudinal half-wave number (m)

In Eqs. (13), $u_{mn}(t)$, $v_{mn}(t)$ and $w_{mn}(t)$ are the time-dependent generalized coordinates. The integers m and n denote the number of longitudinal half-waves and circumferential waves, respectively. The terms $u_{m0}(t)$, $v_{m0}(t)$, and $w_{m0}(t)$ represent the generalized coordinates for the axisymmetric bending modes ($n = 0$). The axial wavenumber λ_m is defined as $\lambda_m = \frac{m\pi}{l}$ [25].

2.4. Fluid Interaction:

The fluid is modeled as incompressible, inviscid, and irrotational, fully contained within the shell with no free surface and no mean flow. The shell is open at both ends and is not a pressurized vessel. For this configuration—a supported cylindrical shell containing a quiescent fluid—the time derivative of the kinetic energy is given by Eq. (14) [11]:

$$\frac{d}{dt}\left(\frac{\partial T}{\partial \dot{q}_i}\right) = \begin{cases} \rho_{shell} h \left(\frac{l}{2}\right) \psi_n R \ddot{q}_i & if\ q_i = u_{mn}\ or\ v_{mn} \\ (\rho_{shell} + \rho_v) h \left(\frac{l}{2}\right) \psi_n R \ddot{q}_i & if\ q_i = w_{mn} \end{cases} \quad (14)$$

where ψ_n and ρ_v are defined as Eqs. (15) [11]:

$$\psi_n = \begin{cases} 2\pi & if\ n = 0 \\ \pi & if\ n > 0 \end{cases} \quad (15a)$$

$$\rho_v = \frac{\rho_F}{k_1 h} \frac{I_n(k_1 R)}{I_n'(k_1 R)} \quad (15b)$$

This potential flow formulation for a stationary, incompressible fluid is a well-established approach for modeling the added-mass effect in vibrating shells and has been successfully validated against experimental results in prior studies of hyperelastic fluid-filled cylindrical shells [29, 44].

2.5. Nonlinear Vibration:

In Eqs. (15), ρ_F denotes the fluid density, I_n is the modified Bessel function of the first kind of order n, $k_1 = \sqrt{\lambda_m^2 - \left(\frac{\omega}{c}\right)^2}$, and c represents the speed of sound in the fluid. Substituting the displacement functions from Eqs. (13) into the Lagrangian formulation (Eq. (8)), followed by analytical simplification, yields the governing equation of motion, Eq. (16) [45]:

$$\boldsymbol{M}\ddot{q}_i + \boldsymbol{C}\dot{q}_i + \boldsymbol{K_L} q_i + \boldsymbol{K} q_j q_i + \boldsymbol{K_{NL1}} q_j q_i^2 + \boldsymbol{K_{NL2}} q_i^3 = 0 \quad (16)$$

The matrices $\boldsymbol{M}$, $\boldsymbol{C}$, and $\boldsymbol{K_L}$ represent the linear mass, damping, and stiffness matrices, respectively. The terms $\boldsymbol{K_{NL1}}$ and $\boldsymbol{K_{NL2}}$ denote the second-order and third-order nonlinear stiffness matrices. While the matrices $\boldsymbol{M}$, $\boldsymbol{C}$, $\boldsymbol{K_L}$, and $\boldsymbol{K_{NL2}}$ are scalars with respect to the generalized coordinates, $\boldsymbol{K_{NL1}}$ may contain off-diagonal terms coupling different coordinates q_j. All matrices are of dimension 6×6, corresponding to the degrees of freedom of the system. Although the governing equations can generate higher-order nonlinear terms beyond cubic (q_i^3), the present analysis is restricted to terms up to the third order. Thus, Eq. (16) can be expressed in the following form:

$$\boldsymbol{M}\ddot{q}_i + \boldsymbol{C}\dot{q}_i + \boldsymbol{K_L} q_i + \boldsymbol{K_{NL1}} q_i^2 + \boldsymbol{K_{NL2}} q_i^3 = 0 \quad (17)$$

The explicit form of the mass matrix is:

$$\begin{bmatrix} M_{11} & 0 & 0 & 0 & 0 & 0 \\ 0 & M_{22} & 0 & 0 & 0 & 0 \\ 0 & 0 & M_{33} & 0 & 0 & 0 \\ 0 & 0 & 0 & M_{44} & 0 & 0 \\ 0 & 0 & 0 & 0 & M_{55} & 0 \\ 0 & 0 & 0 & 0 & 0 & M_{66} \end{bmatrix} \quad (18a)$$

$$M_{11} = M_{33} = \frac{1}{2} h l \pi R \rho \quad (18b)$$

$$M_{22} = M_{44} = h l \pi R \rho \quad (18c)$$

$$M_{55} = \frac{h^3 l n^2 \pi \rho}{24R} + \frac{1}{2} h l \pi R \rho + \frac{h^3 m^2 \pi^3 R \rho}{24 l} \quad (18d)$$

$$M_{66} = h l \pi R \rho + \frac{h^3 m^2 \pi^3 R \rho}{12 l} \quad (18e)$$

The presence of the internal fluid alters only the mass matrix components $\boldsymbol{M}_{55}$ and $\boldsymbol{M}_{66}$, as defined by the modified expressions in Eqs. (19).

$$M_{55} = \frac{h^3 l n^2 \pi \rho_{shell}}{24R} + \frac{1}{2} h l \pi R (\rho_{shell} + \rho_v) + \frac{h^3 m^2 \pi^3 R \rho_{shell}}{12 l} \quad (19a)$$

$$M_{66} = h l \pi R (\rho_{shell} + \rho_v) + \frac{h^3 m^2 \pi^3 R \rho}{12 l} \quad (19b)$$

The damping matrix $\boldsymbol{C}$ is diagonal and is given by Eqs. (20).

$$\begin{bmatrix} C_{11} & 0 & 0 & 0 & 0 & 0 \\ 0 & C_{22} & 0 & 0 & 0 & 0 \\ 0 & 0 & C_{33} & 0 & 0 & 0 \\ 0 & 0 & 0 & C_{44} & 0 & 0 \\ 0 & 0 & 0 & 0 & C_{55} & 0 \\ 0 & 0 & 0 & 0 & 0 & C_{66} \end{bmatrix} \quad (20a)$$

$$C_{11} = C_{33} = C_{55} = \frac{1}{2} c_d l \pi R \rho \quad (20b)$$

$$C_{22} = C_{44} = C_{66} = c_d l \pi R \rho \quad (20c)$$

The linear stiffness matrix $\boldsymbol{K_L}$ is symmetric and has the following form:

$$\begin{bmatrix} K_{L11} & 0 & K_{L13} & 0 & K_{L15} & 0 \\ 0 & K_{L22} & 0 & 0 & 0 & K_{L26} \\ K_{L31} & 0 & K_{L33} & 0 & K_{L35} & 0 \\ 0 & 0 & 0 & K_{L44} & 0 & 0 \\ K_{L51} & 0 & K_{L53} & 0 & K_{L55} & 0 \\ 0 & K_{L62} & 0 & 0 & 0 & K_{L66} \end{bmatrix}_{Linear} \quad (21a)$$

$$K_{L11} = \frac{h\pi(h^2 + 12R^2)(l^2n^2 + 4m^2\pi^2R^2)}{24lR^3}(\mu 1 + \mu 2) \quad (21b)$$

$$K_{L22} = \frac{hm^2\pi^3(h^2 + 12R^2)(\mu 1 + \mu 2)}{3lR} \quad (21c)$$

$$K_{L33} = \frac{h\pi(h^2 + 12R^2)(4l^2n^2 + m^2\pi^2R^2)}{24lR^3}(\mu 1 + \mu 2) \quad (21d)$$

$$K_{L44} = \frac{hm^2\pi^3(h^2 + 12R^2)(\mu 1 + \mu 2)}{12lR} \quad (21e)$$

$$K_{L55} = \frac{hn\pi(12l^2R^2 + h^2(l^2n^2 + m^2\pi^2R^2))}{6lR^3}(\mu 1 + \mu 2) \quad (21f)$$

$$K_{L66} = \frac{h\pi(12l^4 + h^2m^4\pi^4R^2)(\mu 1 + \mu 2)}{3l^3R} \quad (21g)$$

$$K_{L13} = K_{L31} = \frac{-hmn\pi^2(h^2 + 12R^2)}{8R^2}(\mu 1 + \mu 2) \quad (21h)$$

$$K_{L15} = K_{L51} = \frac{-hm\pi^2(12l^2R^2 + h^2(l^2n^2 + m^2\pi^2R^2))}{12l^2R^2}(\mu 1 + \mu 2) \quad (21i)$$

$$K_{L26} = K_{L62} = \frac{hm\pi^2(12l^2 + h^2m^2\pi^2)}{6l^2}(\mu 1 + \mu 2) \quad (21j)$$

$$K_{L35} = K_{L53} = \frac{hn\pi(12l^2R^2 + h^2(l^2n^2 + m^2\pi^2R^2))}{6lR^3}(\mu 1 + \mu 2) \quad (21k)$$

The nonlinear stiffness matrices $\boldsymbol{K_{NL1}}$ and $\boldsymbol{K_{NL2}}$ contain off-diagonal terms that couple different generalized coordinates q_j. These couplings are responsible for internal resonance phenomena in nonlinear vibrations. Since the focus of this study is on the primary nonlinear free vibration response and not on internal resonance, the off-diagonal coupling terms in $\boldsymbol{K_{NL1}}$ and $\boldsymbol{K_{NL2}}$ are neglected. This simplification decouples the equations, rewritten as follows:

$$\boldsymbol{M}\ddot{q}_i + \boldsymbol{C}\dot{q}_i + \boldsymbol{K_L}q_i + \boldsymbol{K_{NL1}}q_i^2 + \boldsymbol{K_{NL2}}q_i^3 = \boldsymbol{0} \quad (22)$$

The domains of the coefficient matrices are considered to be scalar. In the present analysis, internal resonance is not considered. The equations for the asymmetric and axisymmetric modes then decouple into the standard Duffing-type forms given in Eqs. (24) and (25).

2.6. The method of multiple scales:

This section analyzes the steady-state radial vibration of the hyperelastic cylindrical shell using the method of multiple time scales. The system of six nonlinear equations in Eq. (22)—comprising three equations for asymmetric modes and three for axisymmetric modes across the longitudinal, circumferential, and radial directions—is normalized by pre-multiplying by the inverse of the mass matrix, $\mathbf{M}^{-1}$. Due to the diagonal nature of $\mathbf{M}$, this operation yields a decoupled system where all resulting coefficient matrices remain diagonal. The normalized equation of motion is given by:

$$\ddot{q}_i + \boldsymbol{M}^{-1}\boldsymbol{C}\dot{q}_i + \boldsymbol{M}^{-1}\boldsymbol{K_L}q_i + \boldsymbol{M}^{-1}\boldsymbol{K_{NL1}}q_i^2 + \boldsymbol{M}^{-1}\boldsymbol{K_{NL2}}q_i^3 = 0 \quad (23)$$

A key distinction arises between asymmetric and axisymmetric modes: the equations for asymmetric modes lack a quadratic nonlinear term (q_i^2), while those for axisymmetric modes include it. Consequently, the system is solved using two distinct general forms, represented by Eqs. (24) and (25):

$$\ddot{q}_{mn} + M_{mn}^{-1}C_{mn}\dot{q}_{mn} + \omega_L^2 q_{mn} + M_{mn}^{-1}K_{mn}^{NL2}q_{mn}^3 = 0 \quad (24)$$

$$\ddot{q}_{m0} + M_{m0}^{-1}C_{m0}\dot{q}_{m0} + \omega_L^2 q_{m0} + M_{m0}^{-1}K_{m0}^{NL1}q_{mn}^2 + M_{m0}^{-1}K_{m0}^{NL2}q_{mn}^3 = 0 \quad (25)$$

Eqs. (24) and (25) represent the two canonical forms of the nonlinear governing equations for the axisymmetric and asymmetric modes, respectively. These equations are solved analytically using the method of multiple scales.

2.6.1. Asymmetric modes:

Eq. (24), which governs asymmetric modes ($n \neq 0$), takes the general form of a Duffing-type oscillator with viscous damping, given by Eq. (26) [20]:

$$\ddot{q} + 2\mu\dot{q} + \omega_0^2 q + \alpha q^3 = 0 \quad (26)$$

Given that the nonlinearity is cubic (odd-order), a first-order perturbation expansion is sufficient. The time scales are defined as follows [20]:

$$T_0 = t, \qquad T_1 = \epsilon t, \quad (27)$$

Here, T_0 is the fast time scale, and T_1 is the slow time scale, where ϵ is a small dimensionless parameter that orders the magnitude of damping and nonlinearity. The method of multiple scales follows the standard procedure described by Nayfeh & Mook [20]. The solution is expressed as an asymptotic expansion in the perturbation parameter ϵ [20]:

$$q(t) = q_0(T_0, T_1) + \epsilon q_1(T_0, T_1) + O(\epsilon^2) \quad (28)$$

Substituting Eqs. (27) and (28) into Eq. (26) and collecting terms of like powers of ϵ yields the following hierarchy of equations:[20]:

$$O(\epsilon^0): \quad D_0^2 q_0 + \omega_0 q_0 = 0 \quad (29a)$$

$$O(\epsilon^1):\ D_0^2 q_1 + \omega_0 q_1 = -2D_0 D_1 q_0 - 2\mu D_0 q_0 - \alpha q_0^3 \quad (29b)$$

where $D_n = \partial/\partial T_n$. The solution to the zeroth-order problem Eq. (29a) is [20]:

$$q_0 = A(T_1)e^{i\omega_0 T_0} + \bar{A}(T_1)e^{-i\omega_0 T_0} \quad (30)$$

where $A(T_1)$ is a complex-valued amplitude function. Substituting Eq. (30) into the first-order Eq. (29b) gives:

$$D_0^2 q_1 + \omega_0 q_1 = \left[-2i\omega_0 \acute{A} - 2\mu i\omega_0 A - 3\alpha A^2 \bar{A}\right]e^{i\omega_0 T_0} + CC + NST \quad (31)$$

where $A' = dA/dT_1$, CC denotes the complex conjugate, and NST denotes non-secular terms. To eliminate secular terms that lead to unbounded growth, the coefficient of $e^{i\omega_0 T_0}$ must vanish:

$$2i\omega_0\left(\acute{A} + \mu A\right) + 3\alpha A^2 \bar{A} = 0 \quad (32)$$

The complex amplitude A is expressed in polar form:

$$A = \frac{1}{2}a(T_1)e^{i\beta(T_1)}, \qquad \acute{A} = \frac{1}{2}\acute{a}(T_1)e^{i\beta(T_1)} \quad (33)$$

where $a(T_1)$ and $\beta(T_1)$ represent the amplitude and phase, respectively. Substituting Eq. (33) into Eq. (32) and separating real and imaginary parts of Eq. (31) yields the following equations governing the amplitude and phase:

$$\acute{a} = -\mu a \quad (34)$$

$$a\acute{\beta} = \frac{3\alpha}{8\omega_0}a^3 \rightarrow \acute{\beta} = \frac{3\alpha}{8\omega_0}a^2 \quad (35)$$

The solution to the amplitude Eq. (34) is obtained by direct integration:

$$\frac{da}{a} = -\mu dT_1 \rightarrow ln\, a = -\mu T_1 + c \quad (36a)$$

Applying the initial condition $a(0) = a_0$ yields the solution for the amplitude:

$$a(T_1) = a_0 e^{-\mu T_1} \quad (36b)$$

The phase Eq. (35) is solved by substituting Eq. (36b):

$$\acute{\beta} = \frac{3}{8}\frac{\alpha}{\omega_0}a_0^2 e^{-2\mu T_1} \rightarrow \beta = \frac{-3}{16}\frac{\alpha a_0^2}{\omega_0 \mu}e^{-2\mu T_1} + \beta_0 \quad (37)$$

where β_0 is a constant of integration. The first-order approximate solution for the system's response is therefore given by:

$$q(t) = \frac{1}{2}a_0 e^{-\epsilon T_1} exp\left[i\omega_0 t - i\frac{3\alpha a_0^2}{16\omega_0\mu}e^{-2\mu\epsilon t} + i\beta_0\right] + CC \quad (38a)$$

From this solution, the nonlinear natural frequency ω_{NL} is identified as:

$$\omega_{NL} = \omega_{0mn} + \frac{3a_0^2}{8}\frac{\alpha}{\omega_{0mn}}\epsilon \quad (38b)$$

where CC denotes the complex conjugate of the preceding terms. Eq. (38a) reveals that the vibration amplitude decays exponentially as $a_0 e^{-\epsilon\mu t}$, while the nonlinear natural frequency exhibits amplitude-dependent behavior. As shown in Eq. (38b), the nonlinear frequency shift is proportional to the square of the vibration amplitude a_0, demonstrating the characteristic hardening-spring effect of the Duffing oscillator.

2.6.2. Axisymmetric modes:

Equation (39) represents the general form of the nonlinear vibration equation for axisymmetric modes.

$$\ddot{q} + 2\mu\dot{q} + \omega_0^2 q + \alpha_2 q^2 + \alpha_3 q^3 = 0 \quad (39)$$

Due to the presence of the quadratic term, a first-order expansion is insufficient for solving this equation. Therefore, a second-order multiple-scale expansion is employed. The solution is expressed in terms of three time scales:

$$q(t;\epsilon) = q_0(T_0,T_1,T_2) + \epsilon q_1(T_0,T_1,T_2) + \epsilon^2 q_2(T_0,T_1,T_2) + \cdots \quad (40)$$

where the time scales are defined as:

$$T_0 = \epsilon^0 t, \qquad T_1 = \epsilon^1 t, \qquad T_2 = \epsilon^2 t, \quad (41)$$

Substituting the expansion into Eq. (39) and collecting terms of equal powers of ϵ yields the following hierarchy of equations:

$$O(\epsilon^0): D_0^2 q_0 + \omega_0^2 q_0 = 0 \quad (42a)$$

$$O(\epsilon^1): D_0^2 q_1 + \omega_0^2 q_1 = -2D_0 D_1 q_0 - \alpha_2 q_0^2 \quad (42b)$$

$$O(\epsilon^2): D_0^2 q_2 + \omega_0^2 q_2 = -2D_0 D_1 q_1 - 2D_0 D_2 q_0 - D_1^2 q_0 - 2\mu D_0 q_0 - 2\alpha_2 q_0 q_1 - \alpha_3 q_0^3 \quad (42c)$$

The general solution to the zeroth-order Eq. (42a) is:

$$q_0 = A(T_1,T_2)e^{i\omega_0 T_0} + \bar{A}(T_1,T_2)e^{-i\omega_0 T_0} \quad (43)$$

Substituting Eq. (43) into the first-order Eq. (42b) gives:

$$D_0^2 q_1 + \omega_0^2 q_1 = -2i\omega_0 D_1 A e^{i\omega_0 T_0} - \alpha_2[A^2 e^{2i\omega_0 T_0} + A\bar{A}] + cc \quad (44)$$

To eliminate secular terms in Eq. (44), the condition $D_1 A = 0$ must hold, implying that $A = A(T_2)$. The particular solution for q_1 is then:

$$q_1 = \frac{\alpha_2}{\omega_0^2}\left[-2A\bar{A} + \frac{1}{3}A^2 e^{2i\omega_0 T_0} + \frac{1}{3}\bar{A}^2 e^{-2i\omega_0 T_0}\right] \quad (45)$$

Substituting q_0 and q_1 into the second-order Eq. (42c) yields:

$$D_0^2 q_2 + \omega_0^2 q_2 = -\left[2i\omega_0(\acute{A} + \mu A) + \left(3\alpha_3 - \frac{10\alpha_2^2}{3\omega_0^2}\right)A^2\bar{A}\right]e^{i\omega_0 T_0} + CC + NST \quad (46)$$

where the prime (') denotes the derivative with respect to T_2. To eliminate secular terms in q_2, the coefficient of $e^{i\omega_0 T_0}$ must vanish:

$$2i\omega_0(\acute{A} + \mu A) + \left(3\alpha_3 - \frac{10\alpha_2^2}{3\omega_0^2}\right)A^2\bar{A} = 0 \quad (47)$$

Following a solution procedure similar to that for asymmetric modes (but omitted here for brevity), the amplitude and phase are found to be:

$$a = a_0 e^{-\mu T_2} \quad where\ a = a_0 \quad at \quad T_2 = 0 \quad (48a)$$

$$\beta = \left(\frac{9\alpha_3\omega_0^2 - 10\alpha_2^2}{24\omega_0^3}\right) \times \frac{-a_0^2}{2\mu} e^{-2\mu T_2} + \beta_0 \quad (48b)$$

$$A = \frac{1}{2}a_0 e^{-\mu T_2} exp\left[-i\left(\frac{9\alpha_3\omega_0^2 - 10\alpha_2^2}{24\omega_0^3}\right)\frac{a_0^2}{2\mu}e^{-2\mu T_2} + i\beta_0\right] \quad (48c)$$

$$\bar{A} = \frac{1}{2}a_0 e^{-\mu T_2} exp\left[i\left(\frac{9\alpha_3\omega_0^2 - 10\alpha_2^2}{24\omega_0^3}\right)\frac{a_0^2}{2\mu}e^{-2\mu T_2} - i\beta_0\right] \quad (48d)$$

The system's response can be derived by determining q_0 and q_1 from the known values of A and $\bar{A}$. Analysis of the system's response indicates that the damping is very light for this hyperelastic material (8% carbon rubber), with a damping coefficient μ typically ranging from 0.02 to 0.06 [18]. Therefore, to simplify the analysis of the fundamental nonlinear behavior, the damping coefficient is neglected in the subsequent derivation of the nonlinear natural frequency. Ignoring damping, the nonlinear natural frequency for both axisymmetric and asymmetric modes is expressed as follows:

The general form of the equation

$$\ddot{q}_{mn} + \omega_{0mn}^2 q_{mn} + \alpha_3 q^3{}_{mn} = 0 \quad (49a)$$

System's response

$$w_{mn} = a_0\, cos\left[\omega_{0mn}t + \frac{3\alpha_3 a_0^2}{8\omega_{0mn}^2}\epsilon t + \beta_0\right] \quad (49b)$$

Nonlinear Natural Frequency

$$\omega_{NL} = \omega_{0mn} + \frac{3a_0^2}{8}\frac{\alpha}{\omega_{0mn}}\epsilon \quad (49c)$$

For axisymmetric modes:

The general form of the equation

$$\ddot{q}_{m0} + \omega_{0m0}^2 q_{m0} + \alpha_2 q^2{}_{m0} + \alpha_3 q^3{}_{m0} = 0 \quad (50a)$$

System's response

$$w_{m0} = \epsilon a_0\, cos[\omega t + \beta_0] - \left(\frac{\epsilon^2 a_0^2 \alpha_2}{2\omega_0^2}\right)\left[1 - \frac{1}{3}cos(2\omega t + 2\beta_0)\right] \quad (50b)$$

Nonlinear Natural Frequency

$$\omega_{NL} = \omega_{0m0}\left[1 + \frac{9\alpha_3\omega_{0m0} - 10\alpha_2^2}{24\omega_{0m0}^4}\epsilon^2 a_0^2\right] \quad (50c)$$

3. Result and Discussion

The validation strategy involves comparing linear natural frequencies with ANSYS simulations and literature, and nonlinear frequency ratios with both numerical results and published analytical solutions. This study examines the free vibration behavior of a thin-walled cylinder made of hyperelastic material. The analysis is performed twice: once without fluid and once with fluid. The Mooney-Rivlin strain energy density function, Kirchhoff-Love kinematic assumptions, and Novozhilov nonlinear shell theory are used to model the thin-walled shell. The system, characterized by six degrees of freedom, is then investigated using Lagrange's equation. Of these six degrees of freedom, three are associated with axisymmetric modes, and three are associated with asymmetric modes.

First, the linear natural frequency of the system without fluid is obtained and compared

with results from ANSYS finite element software. Subsequently, the linear natural frequency in the presence of fluid is determined. Following this, the nonlinear vibration response is examined for both fluid-filled and empty configurations, and the sensitivity of the system's frequency and amplitude to key geometric and material parameters is investigated. All analyses are performed using the geometric and material properties summarized in Tables 1 and 2, respectively.

Table 1. Geometrical parameters of the thin-walled cylindrical shell

Parameter	Symbol	Value(m)
Radius	R	0.1
Thickness	h	0.0048
Length	L	0.109951

Table 2. Hyperelastic material properties for the two-parameter Mooney-Rivlin model [8]

Poisson's ratio	Density	Modulus of elasticity	Material constant	Material constant
(ν)	(ρ) kgm^{-3}	(E) Pa	$(C_{01}=\frac{\mu_2}{2})$ Pa	$(C_{10}=\frac{\mu_1}{2})$ Pa
0.47	1100	1247060.2	208092.75	-249.4

The finite element analysis was performed using ANSYS software to validate the analytical results. The cylindrical shell was discretized using quadratic shell elements, which are well-suited for thin-walled structures and provide improved accuracy in representing bending behavior compared with linear elements.

Since numerical results may depend on mesh resolution, a mesh sensitivity analysis was carried out to evaluate the convergence of the finite element solution.

It was observed that when the element size reaches approximately 5 mm, further mesh refinement leads to negligible changes in the computed natural frequency. Therefore, the mesh with an element size of 5 mm was adopted for the final simulations as it provides a good balance between computational efficiency and numerical accuracy.

The mesh convergence results demonstrate that the numerical solution is essentially mesh-independent. Consequently, the discretization-related numerical uncertainty is minimized, and the finite element results can be considered reliable for validating the analytical model.

Possible numerical uncertainties in the finite element simulations may arise from mesh discretization, element interpolation characteristics, implementation of boundary conditions, and solver tolerances. In this study, the discretization error was reduced through the mesh convergence analysis described above. Furthermore, consistent boundary conditions were applied in both the analytical and numerical models. The good agreement observed between the analytical predictions and the finite element results confirms the robustness of the numerical model and supports the validity of the analytical formulation.

Table 4 presents a comparison of the linear natural frequencies (Hz) for the simply supported hyperelastic cylindrical shell with longitudinal half-wave numbers m=1and m=2. The present analytical results are compared with ANSYS simulations and published papers, Saeidiha et al. [24] and Zhao et al. [25]. The overall agreement is satisfactory, validating the linear foundation of the proposed model.

Table 3: Mesh convergence study for the finite element model

Element size (mm)	12	11	10	9	8	7	6	5	4
Fundamental frequency (Hz)	30.788	30.762	30.742	30.72	30.701	30.683	30.665	30.645	30.644

Table 4. Comparison of linear natural frequencies (Hz) for a simply supported hyperelastic cylindrical shell

n	0	1	2	3	4	5	6
m	1	1	1	1	1	1	1
Present Work	53.0878	46.2092	35.2198	27.7418	26.0066	29.8191	37.5505
ANSYS	57.023	46.506	34.11	27.732	26.693	30.279	37.364
Saeidiha et al.[24]	53.03	48.65	35.64	28.18	25.38	30.46	39.06
Zhao et al.[25]	54.33	45.58	31.7	26.51	22.38	26.76	35.47
m	2	2	2	2	2	2	2
Present Work	59.9386	58.8029	56.1988	53.9076	53.6315	56.3703	59.9383
ANSYS	59.456	57.962	55.2	52.436	51.772	54.261	59.894
Saeidiha et al.[24]	59.80	58.32	57.03	54.85	53.93	57.63	61.17
Zhao et al.[25]	59.76	58.96	57.68	53.45	53.61	57.14	61.24

Discrepancies between the present analytical model and ANSYS results, particularly for the axisymmetric mode (n=0), are attributed to differences in theoretical foundations. The current model is based on classical Novozhilov shell theory, which neglects rotary inertia and shear deformation effects, whereas ANSYS employs finite elements that account for these higher-order effects. The improved agreement for m=2is due to the shell's behavior becoming more plate-like, reducing the influence of shear deformation. The agreement with the published linear frequencies from Saeidiha et al. [24] and Zhao et al. [25] further confirms the reliability of the present formulation for the linear vibration analysis of hyperelastic cylindrical shells.

3.1. Influence of Shell Length on Natural Frequency

The influence of cylinder length on the natural frequency was analyzed using the parameter β=2R/L, where the shell is considered short if β>1and relatively long if β≤0.5. The system's natural frequencies were compared for three values of β: 0.5, 1, and 1.5. As shown in Figure 3, increasing β (i.e., shortening the shell) resulted in a significant increase in natural frequency and reduced sensitivity to vibrational excitation. Furthermore, this change in geometry altered the fundamental mode shape: the primary mode shifted from (1,2) at β=0.5, to (1,3) at β=1, and finally to (1,4) at β=1.5.

3.2. Influence of Shell Thickness on Natural Frequency

The influence of shell thickness was investigated using the thickness-to-radius ratio $\alpha = h/R$. To satisfy thin-shell theory assumptions, α was maintained below 0.05 [11]. Natural frequencies were computed for four values of α: 0.005, 0.01, 0.02, and 0.03. As shown in Figure 4, the natural frequency remains nearly constant across different circumferential wave numbers n for small values of α. However, as α increases, the frequency becomes more sensitive to n, resulting in pronounced shifts in the frequency spectrum.

3.3. Effect of Fluid on Linear Natural Frequencies

As established, the presence of a stationary, incompressible fluid inside the open-ended shell increases the system's effective mass by contributing to its kinetic energy without altering its stiffness. Figure 5 compares the natural frequencies of the fluid-filled and empty shells, using water as the fluid medium. The results confirm that the natural frequency decreases consistently across all modes when the shell is fluid-filled. This reduction is a direct consequence of the added fluid mass, which lowers the natural frequency according to the fundamental relationship $\omega_n \propto (k/m)^{1/2}$, where the stiffness k remains constant while the mass m increases. The observed reduction in natural frequency due to fluid addition is consistent with the well-documented added-mass effect and aligns with trends reported in numerical and experimental studies of fluid-filled hyperelastic shells [29], where the stationary fluid lowers the system's natural frequencies across all circumferential wave numbers.

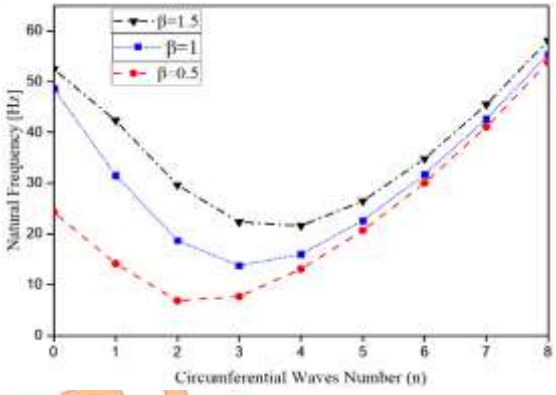

Fig.3. Linear natural frequency vs. circumferential wave number n for different radius-to-length ratios β=2R/L (m=1).

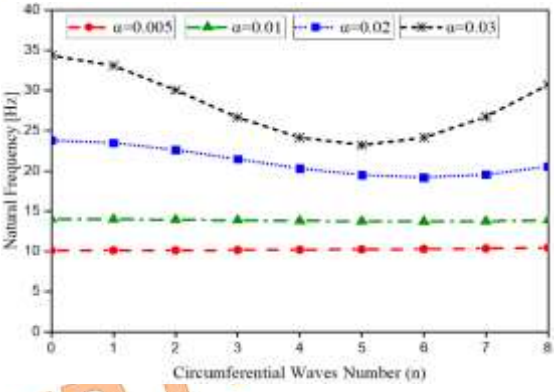

Fig. 4. Linear natural frequency vs. n for various thickness-to-radius ratios α=h/R (m=1).

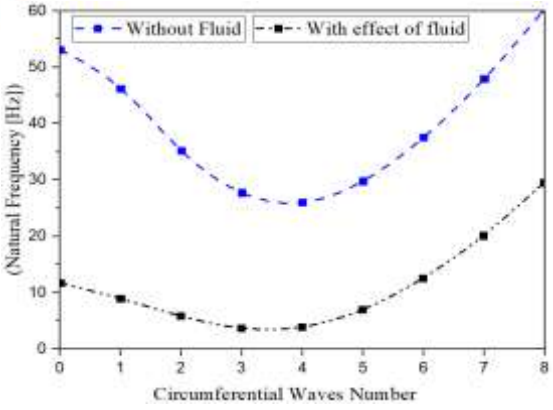

Fig.5. The effect of the presence of fluid on the natural frequency of the system m=1

3.4. Validation of Nonlinear Natural Frequency and Steady-State Response:

To validate the nonlinear vibration solution, the ratio of nonlinear to linear natural frequency ($\frac{\omega_{NL}}{\omega_L}$) was computed and compared against results from ANSYS simulations and established literature sources. Table 4 presents this comparison, where a_0 denotes the vibration amplitude used in the mathematical formulation.

The results show consistent agreement with both ANSYS outputs and values reported in reputable references, with all discrepancies falling within an acceptable error margin. This confirms the accuracy and reliability of the proposed nonlinear solution method.

As evidenced in Table 4, the results obtained in this study align closely with those from references [24, 25], demonstrating the validity of the presented nonlinear vibration analysis.

3.5. Backbone Curve Analysis and Nonlinear Behavior

3.5.1. Comparison of Backbone Curves for Axisymmetric and Asymmetric Modes:

Figure 6 presents the backbone curves for the axisymmetric (1,0) and asymmetric (1,1) modes, both exhibiting hardening behavior—where the nonlinear natural frequency exceeds the linear natural frequency ($\omega_{NL}/\omega_L > 1$). This response stems from the positive third-order nonlinear stiffness coefficients in the system.

The axisymmetric mode demonstrates a stronger hardening effect compared to the asymmetric mode. This difference arises from the influence of the quadratic nonlinear term (governed by α_2) in the axisymmetric equation of motion (Eq. 50c). The negative sign associated with the α_2^2 term in the frequency expression moderates the frequency shift, resulting in a less pronounced increase in nonlinear frequency for the axisymmetric case despite its higher overall hardening magnitude. The stronger hardening in axisymmetric modes arises because axisymmetric deformation induces uniform circumferential stretching, which increases membrane stiffness more effectively than the bending-dominated asymmetric modes.

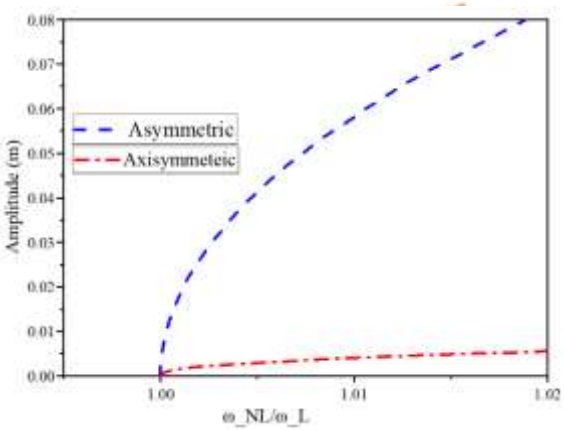

Fig.6. Backbone curves for axisymmetric mode (1,0) and asymmetric mode (1,1), showing amplitude-dependent frequency shift ω_{NL}/ω_L

3.5.2. Influence of Circumferential Wave Number on Asymmetric Modes

Figure 7 demonstrates the effect of increasing the circumferential wave number n on the nonlinear hardening behavior of asymmetric modes. The results indicate a clear trend: as n increases, the hardening behavior becomes more pronounced. Notably, for higher values of n, the nonlinear response converges toward the characteristics observed in the axisymmetric (1,0) mode, suggesting a diminishing distinction between asymmetric and axisymmetric nonlinear behavior at larger circumferential wave numbers. Higher circumferential wave numbers increase the curvature-induced membrane stiffness, leading to more pronounced hardening. This is consistent with the known behavior of shells, where shorter circumferential wavelengths enhance geometric nonlinearity.

Table 4. $\frac{\omega_{NL}}{\omega_L}$ Ratio for a cylinder made of isotropic and homogeneous materials.a_0

(m)	Model number	Present work	Saeidiha et al.[24]	Zhao et al.[25]	ANSYS
0.00254	(1,1)	1.00003	Not Reported	Not Reported	1.00042
	(1,2)	1.00034	1.0006	1.0027	1.00044
	(1,3)	1.0018	1.0058	1.0099	1.00048
	(1,4)	1.00572	1.0331	1.0351	1.002
	(1,5)	1.01351	Not Reported	Not Reported	1.0027

3.5.3. *Influence of Longitudinal Half-Waves on Axisymmetric Modes*

Figure 8 presents the effect of increasing the number of longitudinal half-waves m on the nonlinear response of axisymmetric modes ($n = 0$). The results demonstrate that the hardening behavior intensifies progressively with higher values of m, indicating a strong dependence of nonlinear stiffness on axial modal complexity in axisymmetric vibrations.

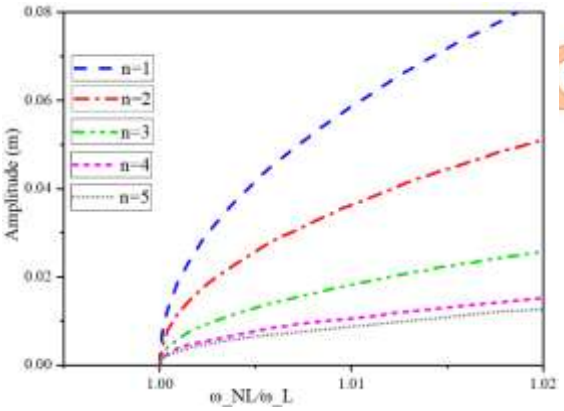

Fig.7. The effect of increasing the circumferential wave number on the system's behaviour in asymmetric modes for m=1.

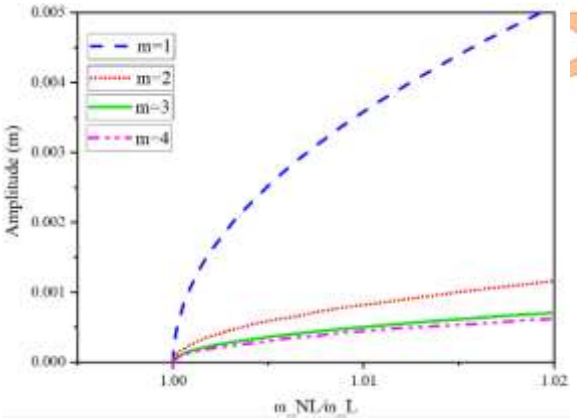

Fig. 8. The effect of increasing the longitudinal half-wave number in symmetric modes

3.5.4. *Effect Length Variation on Nonlinear System Behavior*

The influence of shell length on nonlinear dynamic response was investigated using the radius-to-length ratio $\beta = 2R/L$, where $\beta > 1$ corresponds to short shells and $\beta = 0.5$ to relatively long shells. Figure 9 illustrates the nonlinear frequency-amplitude response for mode (1,1) across four values of β: 0.5, 1, 1.5, and 2. The results reveal a significant dependence of nonlinear behavior on shell length: increasing the length (decreasing β) leads to a transition from hardening to softening behavior. This suggests that longer shells are more prone to nonlinear softening, likely due to enhanced geometric flexibility and reduced structural stiffness relative to shorter, stubbier configurations. Shorter shells (larger β) behave more like rings with greater bending stiffness, leading to hardening. Longer shells (smaller β) exhibit more membrane flexibility, which can promote softening due to larger mid-surface strains.

3.5.5. *Effect of Thickness-to-Radius Ratio on Nonlinear Behavior*

The nonlinear system behavior was examined for the thickness-to-radius ratio $\alpha = h/R$, maintaining $\alpha \leq 0.05$ to satisfy thin-shell theory assumptions. Figure 10 shows the backbone curves for mode (1,1) at four values of α: 0.005, 0.01, 0.02, and 0.05. The results indicate that variations in shell thickness have a negligible influence on the nonlinear hardening behavior. This insensitivity arises because the associated change in structural mass is insignificant for thin-walled configurations, and the primary stiffness characteristics governing the nonlinear response remain largely unaffected by thickness variations within the thin-shell regime.

3.5.6. *Effect of Fluid on Nonlinear Behavior*

The presence of fluid not only reduces the system's natural frequency but also amplifies its nonlinear hardening behavior, as shown in Figure 11. The amplification of hardening behavior due to fluid is attributed to the hydrostatic pressure-induced circumferential prestress, which enhances the geometric stiffness of the shell. This mechanism has been similarly noted in studies on forced vibration of fluid-filled hyperelastic shells, where fluid presence not only adds mass but also modifies the effective nonlinear stiffness [29, 46].

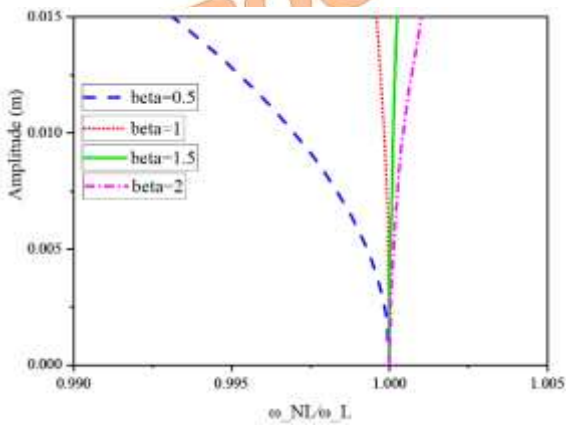

Fig. 9. Effect of shell length (via β=2R/L) on nonlinear frequency–amplitude response for mode (1,1).

3.5.7. *Physical Interpretation of Parametric Effects*

The nonlinear response of the system can be interpreted through two main mechanical mechanisms. First, membrane stiffening caused by in-plane stretching becomes significant in shorter shells and at higher circumferential wave numbers, where geometric nonlinearities intensify the membrane stresses and increase the effective structural stiffness. Second, the presence of internal fluid introduces added mass and fluid-induced prestress, which generally reduces the natural frequencies while modifying the nonlinear stiffness of the system.

As a result, hardening-type behavior becomes more pronounced when geometric nonlinearities (such as higher curvature or shorter shell length) interact with the intrinsic material nonlinearity described by the Mooney–Rivlin model. In contrast, softening behavior tends to appear in longer shells, where increased bending flexibility weakens the membrane restoring mechanism and alters the overall vibration response.

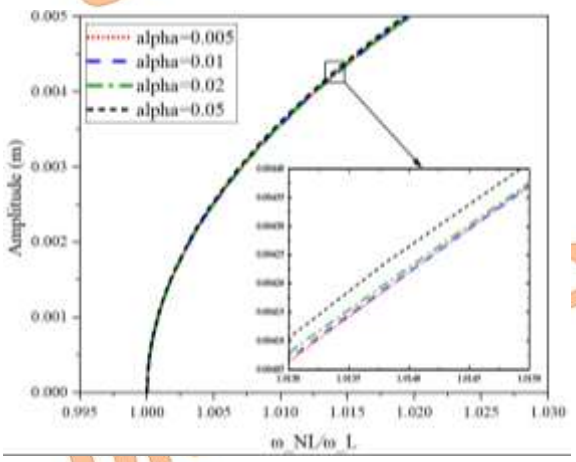

Fig.10. Nonlinear backbone curves for mode (1,1) at various thickness ratios α

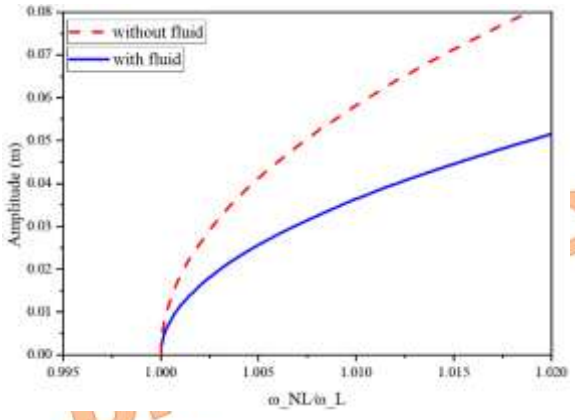

Fig. 11. Comparison of the nonlinear behavior of the system with and without the presence of fluid

4. Conclusions

This study investigated the linear and nonlinear free vibration of fluid-filled, thin-walled cylindrical shells made of hyperelastic material using Novozhilov's nonlinear shell theory and the Mooney–Rivlin constitutive model. The equations of motion were derived via Lagrange's equation, accounting for the kinetic energy of a stationary, incompressible fluid. The system was analyzed with and without fluid, and the results were validated against ANSYS simulations and established literature.

The key findings are summarized as follows:

1. The fundamental vibrational mode was identified as (1,4), corresponding to one longitudinal half wave and four circumferential waves, with the lowest natural frequencies occurring in the radial direction.
2. The radius-to-length ratio (β = 2R/L) significantly influences the dynamics: increasing β stiffens the structure and raises natural frequencies, while decreasing β promotes a transition from hardening to softening nonlinear behavior.
3. Variations in the thickness-to-radius ratio (α = h/R) below the thin shell limit (α ≤ 0.05) have a negligible impact on both linear and nonlinear response due to minimal changes in mass and stiffness.
4. The presence of fluid reduces linear natural frequencies through the added mass effect and enhances nonlinear hardening via hydrostatic pressure-induced circumferential stretching.
5. Nonlinear hardening intensifies with higher circumferential wave number (n), larger numbers of longitudinal half waves (m), and axisymmetric modes (n = 0), owing to stronger membrane contributions and curvature-induced nonlinearities.

Overall, the nonlinear dynamics of hyperelastic cylindrical shells are strongly governed by geometric parameters (R, L, h, m, n) and fluid interaction, with hardening behavior primarily driven by curvature-induced membrane stiffening. The analytical framework developed here provides an effective tool for the design and optimization of systems such as soft robotic actuators and biomedical tubular components.

While the present model captures the essential nonlinear mechanisms of hyperelastic fluid-filled shells, several simplifying assumptions may limit its applicability to complex real-world systems. The fluid is assumed stationary and incompressible, and flow-induced forces, viscosity, and turbulence are not considered. The structural model is based on thin shell theory and small to moderate strain kinematics, which may not fully represent extremely thick shells or large deformation scenarios. In addition, the material behavior is idealized using a Mooney–Rivlin model, and effects such as viscoelasticity, anisotropy, or

time-dependent degradation are not included. Future work could incorporate fluid flow effects, more advanced constitutive models, and experimental validation to extend the applicability of the present analytical framework.

References

[1] Melly, S.K., Liu, L., Liu, Y. & Leng, J., 2021. A review of material models for isotropic hyperelasticity. *International Journal of Mechanical System Dynamics, 1* (1), pp.71-88.

[2] Ricker, A. & Wriggers, P., 2023. Systematic fitting and comparison of hyperelastic continuum models for elastomers. *Archives of Computational Methods in Engineering, 30* (3), pp.2257-2288.

[3] Safi Jahanshahi, A. & Saidi, A.R., 2019. An analytical study on mechanical behavior of human arteries–a nonlinear elastic double layer model. *Scientia Iranica, 26* (4), pp.2431-2440.

[4] Khaniki, H.B., Ghayesh, M.H., Chin, R. & Amabili, M., 2022. A review on the nonlinear dynamics of hyperelastic structures. *Nonlinear Dynamics, 110* (2), pp.963-994.

[5] Khaniki, H.B., Ghayesh, M.H., Chin, R. & Amabili, M., 2023. Hyperelastic structures: A review on the mechanics and biomechanics. *International Journal of Non-Linear Mechanics, 148*, pp.104275.

[6] Khaniki, H.B., Ghayesh, M.H., Chin, R. & Chen, L.-Q., 2022. Experimental characteristics and coupled nonlinear forced vibrations of axially travelling hyperelastic beams. *Thin-walled structures, 170*, pp.108526.

[7] Chen, W., Wang, L. & Dai, H., 2020. Nonlinear free vibration of hyperelastic beams based on neo-hookean model. *International Journal of Structural Stability and Dynamics, 20* (01), pp.2050015.

[8] Breslavsky, I.D., Amabili, M. & Legrand, M., 2014. Nonlinear vibrations of thin hyperelastic plates. *Journal of Sound and Vibration, 333* (19), pp.4668-4681.

[9] Khaniki, H.B., Ghayesh, M.H. & Chin, R., 2023. Theory and experiment for dynamics of hyperelastic plates with modal interactions. *International Journal of Engineering Science, 182*, pp.103769.

[10] Khorshidi, S., Saber-Samandari, S. & Salehi, M., 2020. Free vibration response of functionally graded carbon nanotube double curved shells and panels with piezoelectric layers in a thermal environment. *Scientia Iranica, 27* (5), pp.2391-2408.

[11] Amabili, M., 2008. *Nonlinear vibrations and stability of shells and plates*. Cambridge University Press.

[12] Amabili, M., 2003. A comparison of shell theories for large-amplitude vibrations of circular cylindrical shells: Lagrangian approach. *Journal of Sound and Vibration, 264* (5), pp.1091-1125.

[13] Amabili, M., 2011. Nonlinear vibrations of laminated circular cylindrical shells: Comparison of different shell theories. *Composite Structures, 94* (1), pp.207-220.

[14] Alijani, F. & Amabili, M., 2014. Non-linear vibrations of shells: A literature review from 2003 to 2013. *International journal of non-linear mechanics, 58*, pp.233-257.

[15] Mohamadi, A., Shahgholi, M. & Ghasemi, F.A., 2020. Nonlinear vibration of axially moving simply-supported circular cylindrical shell. *Thin-Walled Structures, 156*, pp.107026.

[16] Zippo, A., Barbieri, M., Iarriccio, G. & Pellicano, F., 2020. Nonlinear vibrations of circular cylindrical shells with thermal effects: An experimental study. *Nonlinear Dynamics, 99*, pp.373-391.

[17] Amabili, M., 2018. *Nonlinear mechanics of shells and plates in composite, soft and biological materials*. Cambridge University Press.

[18] Doedel, E., Champneys, A., Fairgrieve, T., Kuznetsov, Y.A., Sandstede, B. & Wang, X., 1997. Continuation and bifurcation software for ordinary differential equations. *FTP from pub/doedel/auto*.

[19] Asghari, H. & Dardel, M., 2020. Parameter converting method for bifurcation analysis of nonlinear dynamical systems. *Scientia Iranica, 27* (1), pp.310-329.

[20] Nayfeh, A.H. & Mook, D.T., 2008. *Nonlinear oscillations*. John Wiley & Sons.

[21] Dalir, M.A., 2019. Exact mathematical solution for nonlinear free transverse vibrations of beams. *arXiv preprint arXiv:1901.06519*.

[22] Arani, M.S., Bakhtiari, M. & Lakis, A.A., 2023. Analyzing softening and hardening behavior in vibration of a thin incompressible hyperelastic cylindrical shell. *Thin-Walled Structures, 189*, pp.110943.

[23] Arani, M.S., Bakhtiari, M., Toorani, M. & Lakis, A.A., 2024. Studying the nonlinear response of incompressible hyperelastic thin circular cylindrical shells with

geometric imperfections. *Journal of the Mechanical Behavior of Biomedical Materials, 155*, pp.106562.

[24] Saeidiha, M., Ahmadi, H. & Jalali, A., 2023. Nonlinear vibrations analysis of hyperelastic cylindrical shells utilizing the method of multiple scales. *International Journal of Structural Stability and Dynamics*, pp.2450209.

[25] Zhao, W., Zhang, J., Zhang, W. & Yuan, X., 2021. Internal resonance characteristics of hyperelastic thin-walled cylindrical shells composed of mooney–rivlin materials. *Thin-Walled Structures, 163*, pp.107754.

[26] Zhang, J., Xu, J., Yuan, X., Ding, H., Niu, D. & Zhang, W., 2019. Nonlinear vibration analyses of cylindrical shells composed of hyperelastic materials. *Acta Mechanica Solida Sinica, 32*, pp.463-482.

[27] Zhang, J., Zhang, W. & Zhang, Y., 2023. Nonlinear resonant responses of hyperelastic cylindrical shells with initial geometric imperfections. *Chaos, Solitons & Fractals, 173*, pp.113709.

[28] Xu, J., Yuan, X., Zhang, H., Ma, M. & Zhao, W., 2022. Internal resonance of hyperelastic thin-walled cylindrical shells under harmonic axial excitation and time-varying temperature field. *Thin-Walled Structures, 175*, pp.109256.

[29] Zhang, J., Guo, X., Zhang, Y., Zhang, W. & Li, H., 2025. Vibration behaviors of fluid-filled rubber cylindrical shell with different constitutive models: Hyperelasticity and linearity. *Thin-Walled Structures*, pp.113904.

[30] Ghasemi, A.R. & Meskini, M., 2024. A comprehensive study on the free vibration of adhesive lap joint laminated conical–conical shells adherends. *Journal of Vibration and Control, 30* (17-18), pp.4021-4034.

[31] Ghasemi, A.R. & Meskini, M., 2026. Free vibration analysis of adhesively bonded lap joints in laminated composite conical shells with variable thickness and partial geometry adherends. *Journal of Vibration Engineering & Technologies, 14* (1), pp.42.

[32] Meskini, M. & Ghasemi, A.R., 2023. Free vibration analysis of laminated cylindrical adhesive joints with conical composite shell adherends. *Journal of Vibration and Control, 29* (15-16), pp.3475-3491.

[33] Meskini, M. & Ghasemi, A.R., 2021. Electro-magnetic potential effects on free vibration of rotating circular cylindrical shells of functionally graded materials with laminated composite core and piezo electro-magnetic two face sheets. *Journal of Sandwich Structures & Materials, 23* (7), pp.2772-2797.

[34] Ghasemi, A.R. & Mohandes, M., 2020. Free vibration analysis of micro and nano fiber-metal laminates circular cylindrical shells based on modified couple stress theory. *Mechanics of Advanced Materials and Structures, 27* (1), pp.43-54.

[35] Païdoussis, M. & Denise, J.-P., 1972. Flutter of thin cylindrical shells conveying fluid. *Journal of Sound and Vibration, 20* (1), pp.9-26.

[36] Amabili, M. & Paı¨ Doussis, M.P., 2003. Review of studies on geometrically nonlinear vibrations and dynamics of circular cylindrical shells and panels, with and without fluid-structure interaction. *Appl. Mech. Rev., 56* (4), pp.349-381.

[37] Zhang, J., Zhang, W. & Zhang, Y., 2024. Nonlinear resonant analyses of graphene oxide powder reinforced hyperelastic cylindrical shells containing flowing-fluid. *Thin-Walled Structures, 203*, pp.112248.

[38] Khorshidi, K., Savvafi, S. & Zobeid, S., 2025. Investigation of free vibration in fluid-loaded cylindrical shells with a three-layer sandwich wall and an auxetic central layer. *Mechanics of Advanced Composite Structures, 12* (1), pp.53-72.

[39] Breslavsky, I.D. & Amabili, M., 2018. Nonlinear vibrations of a circular cylindrical shell with multiple internal resonances under multi-harmonic excitation. *Nonlinear Dynamics, 93*, pp.53-62.

[40] Wang, G., Li, Y., Qu, Y., Xie, F. & Gao, H., 2024. Internal resonance induced nonlinear vibration and acoustic radiation of a hyperelastic cantilever structure immersed in fluid. *International Journal of Non-Linear Mechanics, 159*, pp.104603.

[41] Ariatapeh, M.Y., Shariyat, M. & Khosravi, M., 2023. Analytical-based exact-kernel vibration and long-term creep stress and large deformation redistributions of the suddenly pressurized incompressible visco-hyperelastic thick cylinders. *International Journal of Non-Linear Mechanics, 151*, pp.104383.

[42] Breslavsky, I.D., Amabili, M. & Legrand, M., 2014. Physically and geometrically non-linear vibrations of thin rectangular plates. *International Journal of Non-Linear Mechanics, 58*, pp.30-40.

[43] Khorshidi, K., Savvafi, S. & Zobeid, S., 2024. Forced vibration of a three-layer cylindrical shell with an auxetic core containing fluid under the influence of shock load using high-order shear deformation theories. *Mechanic of Advanced and Smart Materials, 3* (4)**,** pp.431-464.

[44] Amabili, M., Balasubramanian, P. & Ferrari, G., 2016. Travelling wave and non-stationary response in nonlinear vibrations of water-filled circular cylindrical shells: Experiments and simulations. *Journal of Sound and Vibration, 381***,** pp.220-245.

[45] Khorshidi, K., Soltannia, B., Karimi, M. & Ghorbani, A., 2023. Nonlinear vibration of electro-rheological sandwich plates, coupled to quiescent fluid. *Ocean Engineering, 271***,** pp.113730.

[46] Balasubramanian, P., Ferrari, G. & Amabili, M., 2020. Nonlinear vibrations of a fluid-filled, soft circular shell: Experiments and system identification. *Nonlinear Dynamics, 102* (3)**,** pp.1409-1418.